


## RESEARCH ARTICLE

## Multimodal spatial gradients to explain regional susceptibility to fibrillar tau in Alzheimer's disease

Ying Luan<sup>1,2</sup> | Lukai Zheng<sup>2</sup> | Jannis Denecke<sup>2</sup> | Amir Dehsarvi<sup>2</sup> |  
 Sebastian N. Roemer-Cassiano<sup>2</sup> | Anna Dewenter<sup>2</sup> | Anna Steward<sup>2</sup> |  
 Sergey Shcherbinin<sup>3</sup> | Diana Otero Svaldi<sup>3</sup> | Vikas Kotari<sup>3</sup> | Ixavier Alonzo Higgins<sup>3</sup> |  
 Michael J. Pontecorvo<sup>3</sup> | Carolina Valentim<sup>2</sup> | Julia A. Schnabel<sup>4,5,6</sup> |  
 Francesco Paolo Casale<sup>4</sup> | Martin Dyrba<sup>7</sup> | Stefan Teipel<sup>7,8</sup> | Nicolai Franzmeier<sup>2,9,10</sup> |  
 Michael Ewers<sup>2</sup>  | for the Alzheimer's Disease Neuroimaging Initiative (ADNI)

<sup>1</sup>Department of Radiology, Zhongda Hospital, School of Medicine, Southeast University, Nanjing, China<sup>2</sup>Institute for Stroke and Dementia Research (ISD), University Hospital, Ludwig Maximilian University (LMU), Munich, Germany<sup>3</sup>Eli Lilly and Company, Indianapolis, Indiana, USA<sup>4</sup>Institute of Machine Learning in Biomedical Imaging, Helmholtz Munich, Neuherberg, Germany<sup>5</sup>TUM School of Computation, Information and Technology & TUM Institute for Advanced Study, Technical University of Munich, Munich, Germany<sup>6</sup>School of Biomedical Engineering and Imaging Sciences, King's College London, Strand, London, UK<sup>7</sup>German Center for Neurodegenerative Diseases (DZNE), Rostock, Germany<sup>8</sup>Department of Psychosomatic Medicine, Rostock University Medical Center, Rostock, Germany<sup>9</sup>Munich Cluster for Systems Neurology (SyNergy), Munich, Germany<sup>10</sup>Department of Psychiatry and Neurochemistry, The Sahlgrenska Academy, Institute of Neuroscience and Physiology, University of Gothenburg, Gothenburg, Sweden

## Correspondence

Michael Ewers and Ying Luan, Institute for Stroke and Dementia Research (ISD), University Hospital, Ludwig Maximilian University (LMU), Feodor-Lynen-Street 17, Munich, 81377, Germany.  
 Email: [Michael.ewers@med.uni-muenchen.de](mailto:Michael.ewers@med.uni-muenchen.de) and [yingluan@seu.edu.cn](mailto:yingluan@seu.edu.cn)

## Funding information

National Natural Science Foundation of China, Grant/Award Number: 82202131; Bundesministerium für Bildung und Forschung, Grant/Award Number: 01KU2203; National Institutes of Health, Grant/Award Number: U01 AG024904; Department of Defense, Grant/Award Number: W81XWH-12-2-0012; National Institute on Aging; National Institute of Biomedical Imaging, and Bioengineering

## Abstract

**INTRODUCTION:** In Alzheimer's disease (AD), fibrillar tau gradually progresses from initial seed to larger brain area. However, those brain properties underlying the region-dependent susceptibility to tau accumulation remain unclear.

**METHODS:** We constructed multimodal spatial gradients to characterize molecular properties and connectomic architecture. A predictive model for regional tau deposition was developed by integrating embeddings in the principal gradients of global connectome gradients with gene expression, neurotransmitters, myelin, and amyloid-beta. The model was trained on amyloid-beta-positive participants from Alzheimer's Disease Neuroimaging Initiative (ADNI) and externally validated in independent datasets.

**RESULTS:** The combination of gradients explained up to 77.7% of cross-sectional and 77.3% of longitudinal inter-regional variance of tau deposition. Gene set enrichment

This is an open access article under the terms of the [Creative Commons Attribution-NonCommercial](https://creativecommons.org/licenses/by-nc/4.0/) License, which permits use, distribution and reproduction in any medium, provided the original work is properly cited and is not used for commercial purposes.

© 2025 The Author(s). *Alzheimer's & Dementia* published by Wiley Periodicals LLC on behalf of Alzheimer's Association.

analysis of a major gene expression gradient points to synaptic transmission to confer increased susceptibility to tau.

**DISCUSSION:** Our findings reveal a spatially heterogeneous molecular landscape shaping regional susceptibility to tau deposition, presenting a powerful system-level explanatory model of tau pathology in AD.

#### KEYWORDS

Alzheimer's disease, functional connectivity, gene expression, multimodal gradients, predictive model, neurotransmitters, tau positron emission tomography

#### Highlights

- Spatial gradients of fundamental molecular brain properties associated with tau pathology.
- The explanatory power showed high consistency across studies.
- Genetic analyses suggested that synapse expression plays a vital role in tau accumulation.

## 1 | BACKGROUND

Alzheimer's disease (AD) is the leading cause of dementia in individuals over 65 years.<sup>1</sup> Hallmark pathologies include the deposition of the amyloid-beta ( $A\beta$ ) plaques and fibrillar-tau tangles in the brain. In particular, fibrillar tau is closely associated with neuronal loss and cognitive decline<sup>2</sup> and, thus, constitutes a key driver of dementia symptoms in AD. Fibrillar tau gradually accumulates in the brain, occurring first preferentially in the medial temporal lobe, before spreading to neocortical areas, with sensorimotor cortices remaining relatively spared until late stages.<sup>3–5</sup> However, those factors that underlie a region-specific gradual progression of tau pathology in AD have not been well understood to date, presenting an important research gap for two reasons: First, we need better explanatory models of tau progression toward individualized prediction of disease progression. Second, the identification of brain features that contribute to the regional susceptibility to tau pathology paves the way to identify novel treatment targets to halt the progression of tau in the brain. Therefore, an urgent need remains for developing comprehensive models to understand how local tissue properties and global brain architecture drive regional progression of tau pathology in AD.

Great progress has been made during recent years in modelling tau patterns as a function of the brain's connectome.<sup>6</sup> Findings from multimodal imaging matching tau-deposition to networks of connected brain regions suggest that fibrillar tau is preferentially increased in those brain regions that are closely connected to "epicenters" in which fibrillar tau pathology emerges early in the disease.<sup>7–9</sup> These observations suggest that tau progresses from initial seed regions of tau to other brain regions along functional and structural connections, poten-

tially arising from trans-synaptic transmission and spreading along axonal connections observed in neuronal culture and in vivo mouse models.<sup>5,10,11</sup> However, recent findings from longitudinal modelling studies suggest that in addition to connectivity-dependent spread of tau, the rate of local tau production is an important factor in driving regional tau accumulation.<sup>12</sup> Consequently, a recent framework for modelling tau progression calls for the need to integrate regional susceptibility factors and connectivity to explain regional tau patterns.<sup>13</sup> Along these lines, recent studies employing transcriptomic gene expression maps from the human brain demonstrated that regional expression of MAPT and AD-risk genes are associated with regional tau deposition in AD,<sup>14–16</sup> and contributes to explain regional tau-positron emission tomography (tau-PET) deposition levels.<sup>17,18</sup> However, a systematic evaluation of combined local molecular tissue properties and connectivity to uncover factors that shape regional vulnerability to tau deposition in AD remains to be conducted. The availability of brain maps charting the rich tissue texture composed of features such as transcriptomic gene expression,<sup>19</sup> neurotransmitter systems,<sup>20</sup> glucose consumption, and myelination<sup>21,22</sup> provides an unprecedented opportunity to investigate the susceptibility to pathologies in aging and disease.<sup>23–25</sup> Here, we computed spatial gradients of the brain's molecular and connectomic architecture,<sup>26</sup> and employed gradient distance from epicenter of tau to explain regional differences in the susceptibility to tau deposition. We used gene set enrichment analysis applied to the most important gene expression gradients to identify biological pathways associated with tau deposition. We thus aimed to enhance the explanatory power of local tau deposition and to discover pathways that are conducive to tau deposition.

## 2 | METHODS

### 2.1 | Participants

#### 2.1.1 | Alzheimer's disease neuroimaging initiative (ADNI)

ADNI is an observational multicenter study on the investigation of biomarker and cognitive changes in Alzheimer's disease,<sup>27</sup> where the data are freely available to researchers (<http://adni.loni.usc.edu/>). We included 351 participants with abnormal global amyloid-PET binding ( $A\beta+$ ), including 153 cognitively normal (CN), 128 participants with mild cognitive impairment (MCI), and 70 AD dementia patients from ADNI (recruitment wave 3) based on availability of baseline T1-weighted MRI, 18F-florbetapir (AV-45) or 18F-florbetaben amyloid-PET, and at least one 18F-flortaucipir (AV-1451) tau-PET scan. The T1-weighted MRI, amyloid-PET, and the first flortaucipir image were obtained within the same study visit. Apart from these samples with tau-PET scans, we included two additional samples from ADNI for the computation of gradient images to be used later for the prediction of tau-PET regional values (see section "Calculation of multimodal gradient distance" below), comprising 18F-florbetapir amyloid-PET scans from an additional 467  $A\beta+$  subjects and 18F-fluorodeoxyglucose (FDG)-PET images from 211 CN  $A\beta-$  subjects. The clinical diagnostic criteria in ADNI were described previously.<sup>28</sup> The  $A\beta$  status ( $A\beta+$ ) was quantitatively determined according to pre-established cutoff values for abnormal global amyloid-PET accumulation ( $A\beta+$ , florbetapir PET standardized uptake value ratio [SUVR] > 1.11, or global florbetaben PET SUVR > 1.08 as determined by the ADNI PET core group; for details see <https://tinyurl.com/3jjn7mu7> and <https://tinyurl.com/5yfe9rny>).

#### 2.1.2 | Anti-amyloid treatment in asymptomatic Alzheimer's study (A4)

As an independent validation sample, 392  $A\beta+$  CN subjects who completed 18F-florbetapir PET and 18F-flortaucipir PET were included from the baseline assessment in the A4 study, which is a completed clinical trial on the effect of the anti-amyloid investigational drug solanezumab against cognitive decline in  $A\beta+$  cognitively normal elderly individuals.<sup>29</sup>  $A\beta+$  was defined as global florbetapir PET SUVR > 1.15.<sup>30</sup> The SUVR of 1.10–1.15 was considered to be  $A\beta+$  only when a visual reading of images was also considered to be positive by a two-reader consensus determination.<sup>30</sup>

#### 2.1.3 | The Avid 18F-AV1451-A05 study (A05)

We included a total of 148  $A\beta+$  subjects with MCI or AD dementia from an observational clinical trial "18F-AV1451-A05" (henceforth referred to "A05"; NCT0201650).<sup>31,32</sup> The sample comprised 83 MCI  $A\beta+$  and 65 AD dementia  $A\beta+$  patients (for the clinical diagnostic criteria see).<sup>32</sup>

### RESEARCH IN CONTEXT

1. **Systematic review:** The authors reviewed relevant literatures by searching in PubMed. The current study builds on prior studies relating the human connectome or gene expression to spatial patterns of tau deposition patterns in Alzheimer's disease (AD). However, a comprehensive mapping of diverse regional brain properties and connectomics to explain tau pathology has been lacking so far.
2. **Interpretation:** A multimodal cross-validated gradient-based model was developed that could substantially increase explained variance in regional tau–positron emission tomography (tau-PET) accumulation in AD. The results suggest a disease-stage dependent contribution of different brain properties to regional susceptibility of tau pathology that is shaped by a complex molecular and connectomic landscape.
3. **Future directions:** Further studies are needed to translate the predictive model combining multimodal properties into clinical applications to better understand the heterogeneity of AD at the individual level and advance personalized medicine.

The  $A\beta$  status was determined based on visual rating of florbetapir PET images by two experienced readers.<sup>31,32</sup> The study was approved by the centers' institutional review boards. All subjects or their authorized representatives provided signed informed consent.

All studies were conducted in accordance with the Declaration of Helsinki and the International Conference on Harmonization (ICH) good clinical practice (GCP) guideline. Ethical approval was obtained, and written informed consent was completed by all participants prior to participation.

### 2.2 | Study design

As shown in Figure 1A. The 351  $A\beta+$  subjects from ADNI were randomly split, with 70% of the subjects as a training sample ( $n = 246$ ) and 30% of the subjects as a test sample ( $n = 105$ ). There was no significant difference in age, sex, years of education, apolipoprotein E (APOE)  $\epsilon 4$  status, or clinical classification (CN, MCI, or AD dementia) between the training and test samples. The training sample was used for predictor selection and model training, while the ADNI test sample, and the A4 and A05 data were used for validation. All analyses were performed by stratifying based on clinical diagnosis. For cross-sectional analyses, CN  $A\beta+$  and MCI/dementia  $A\beta+$  subjects in the ADNI training sample were used separately for parameter estimation resulting in disease stage specific models, and CN  $A\beta+$  subjects of A4 and MCI/dementia  $A\beta+$  subjects of A05 samples were used for external validation,

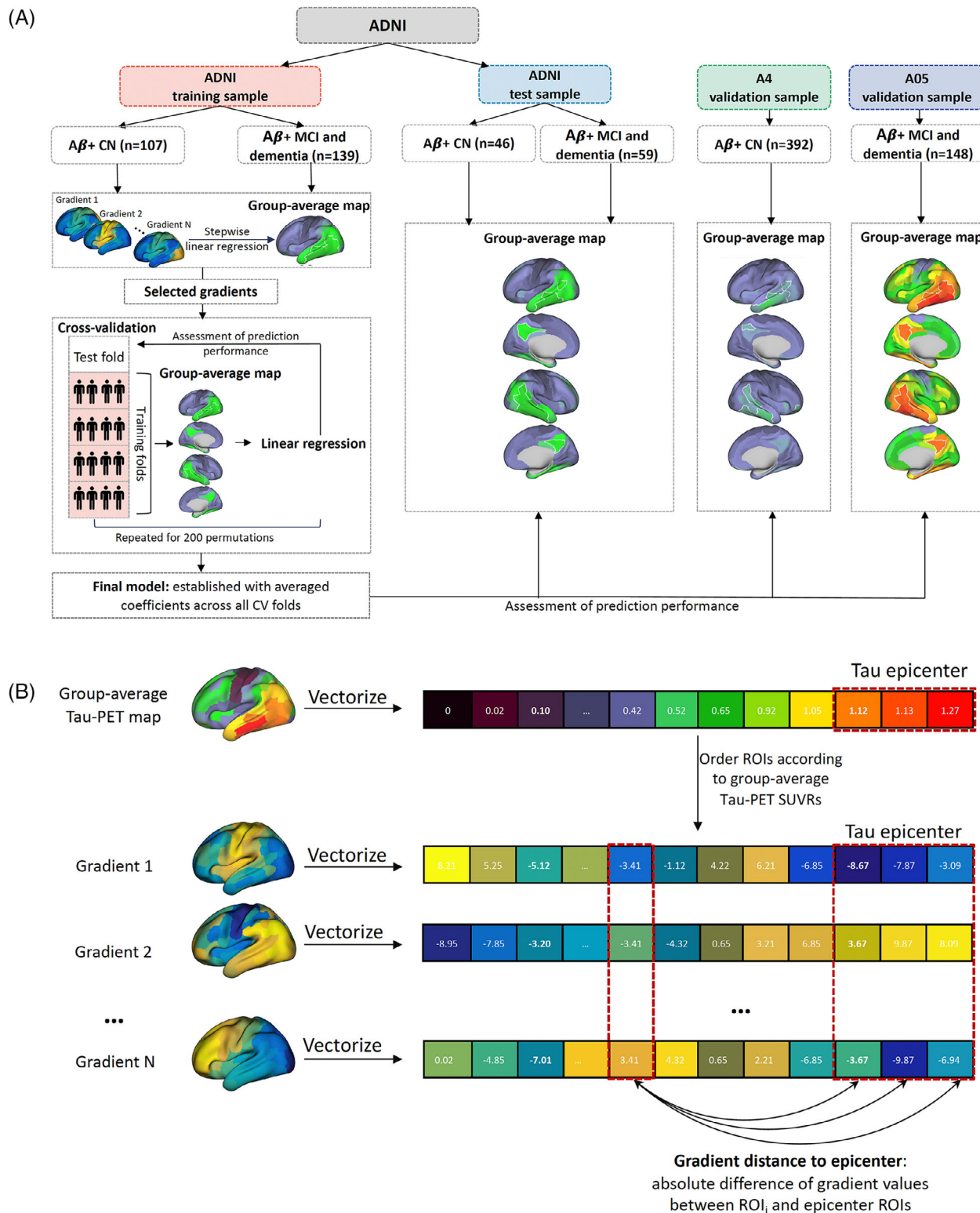


**FIGURE 1** Flow-chart of the analysis pipeline. (A) Subjects from ADNI were randomly split into a training sample ( $n = 246$ ) and a test sample ( $n = 105$ ). In the ADNI training sample, stepwise linear regression was performed to select those predictors which significantly contribute to prediction. For the final model, the coefficients of the predictors were averaged across folds and applied to the non-seen validation samples including ADNI-test, A4, and A05 to assess the prediction performance. (B) Calculation of epicenter-based gradient distance. Tau epicenters were defined as top 10% ROIs showing highest tau-PET levels in the ADNI training sample. For each gradient, the epicenter-based gradient distance was computed as the average absolute difference of the gradient values between tau epicenter ROIs and each ROI across the brain. ADNI, Alzheimer's Disease Neuroimaging Initiative; ROI, region of interest.

respectively. Longitudinal tau-PET data in both training and validation data sets were available in a subset of MCI A $\beta$ + subjects, including 58 subjects from the pooled ADNI dataset (training sample) and in 46 MCI A $\beta$ + from A05 (external validation sample).

## 2.3 | Multimodal neuroimages

### 2.3.1 | MRI and PET acquisition

For the ADNI data set, all MR images were acquired on 3T MRI scanners according to a standardized protocol with a three-dimensional (3D) T1-weighted MPRAGE sequence with 1-mm isotropic voxel size (<http://adni.loni.usc.edu/wp-content/uploads/2017/07/ADNI3-MRI-protocols.pdf>). Tau-PET was recorded 75–105 min (six 5-min time blocks) after injection of the 18F-flortaucipir tracer. The tau-PET images were realigned and averaged into a single image for each subject (see <http://adni.loni.usc.edu/methods/pet-analysis-method/pet-analysis/#pet-pre-processing-container>). Amyloid-PET scans were acquired during 4  $\times$  5 min frames measured 50–70 min post injection of the 18F-florbetapir tracer, or 90–110 min post injection of 18F-florbetaben tracer. The partially preprocessed amyloid-PET images with standard orientation, voxel size, and resolution were downloaded from the ADNI data bank (<http://adni.loni.usc.edu/methods/pet-analysismethod/pet-analysis/>). FDG-PET data were acquired during 6  $\times$  5 min frames started 30 min post injection. The partially preprocessed images with standard orientation, voxel size, and resolution were downloaded (<http://adni.loni.usc.edu/methods/pet-analysismethod/pet-analysis/>). For the A4 study, 3D T1 weighted images were acquired on 3T scanners across clinical sites. Tau-PET was acquired using the 18F-flortaucipir tracer. Amyloid-PET scans were acquired 50 min after injection of 10 mCi of the 18F-florbetapir tracer. For the A05 study, structural 3D T1-weighted MRI images were acquired across clinical sites. 18F-flortaucipir PET images were acquired 80–100 min after tracer injection (in four 5-min frames) and averaged into subject-level single images. Twomin long frames of amyloid-PET scans were acquired for 10 min, beginning 50 min after injection of 370 MBq of the 18F-florbetapir tracer.

### 2.3.2 | MRI and PET processing

All images were screened for artifacts before preprocessing, and processing was conducted independently for each sample (i.e., ADNI vs. A4). T1-weighted structural MRI scans were bias-corrected, segmented, and non-linearly warped to Montreal Neurological Institute (MNI) space using the CAT12 toolbox (<https://neuro-jena.github.io/cat12-help/>). Dynamically acquired PET images were realigned and averaged to obtain single images, which were rigidly registered to the T1-weighted MRI scan. Reference regions (i.e., eroded cerebral white matter for flortaucipir, whole cerebellum for florbetapir, pons for FDG-PET)<sup>33,34</sup> and the cortical Schaefer atlas including 200 regions of interest (ROIs) were warped from MNI to T1-native space, using

the CAT12-derived non-linear normalization parameters. The Schaefer atlas was masked with subject-specific gray matter and applied to PET data to determine SUVRs for each region of the 200 ROIs.<sup>35</sup> ROI harmonization was performed for PET data from ADNI using the neuroCombat toolbox to remove potential effect of site and scanner.<sup>36</sup> ROI-to-ROI pairwise Spearman correlations across subjects were computed each for amyloid-PET ( $n = 467$  A $\beta$ + subjects from ADNI) and FDG-PET ( $n = 211$  CN A $\beta$ - subjects from ADNI), resulting in a single 200  $\times$  200 matrix each for the amyloid-PET and FDG-PET modality for the computation of gradient maps as described below in the section of “Calculation of multimodal gradient distance”. For the A05 data set, all MR and PET images were preprocessed in Avid Radiopharmaceuticals as described previously.<sup>31,32</sup> Briefly, structural T1 weighted images underwent tissue segmentation and spatial normalization to standard MNI space using the SPM8 algorithm. Tau-PET images were co-registered to individual T1-weighted images and spatially normalized to MNI space with FMRIB's Nonlinear Image Registration Tool (FNIRT). SUVR values were calculated by intensity normalization with inferior cerebellar gray as the reference region. ROI-level tau-PET values were subsequently extracted based on the 200 cortical-ROI-Schaefer atlas.

### 2.3.3 | Functional connectivity

To generate a functional network connectivity template, we downloaded the minimally preprocessed 3T resting-state fMRI images from 1000 subjects of the Human Connectome Project (HCP, <http://www.humanconnectomeproject.org/>). As described previously,<sup>7</sup> all fMRI data further underwent the following preprocessing procedures: detrending, band-pass filtering (0.01–0.08 Hz), despiking, and motion scrubbing (i.e., the volumes with framewise displacement exceeding 0.5 mm together with one preceding and two subsequent volumes were replaced with zero-padded volumes). The mean timeseries were extracted for each ROI from Schaefer 200-ROI fMRI atlas by averaging the signal across the voxels within each ROI. Fisher-z transformed Pearson-moment correlations between the fMRI BOLD time series between each pair of the ROIs were calculated to generate a functional connectivity matrix for each subject. To obtain a single, representative connectivity template (200  $\times$  200 ROIs), the group average connectivity matrix across the 1000 HCP subjects was computed.

### 2.3.4 | Gene expression

Whole-brain gene expression maps of a total of 18,686 genes were downloaded (<http://www.meduniwien.ac.at/neuroimaging/mRNA.html>), where the mRNA levels of each gene were interpolated throughout the brain cortex in MNI space as described previously.<sup>37</sup> In brief, the microarray data obtained from the Allen Human Brain Atlas (AHBA)<sup>38</sup> underwent the following processing: (1) spatial registration to MNI space; (2) inter-hemispheric registration; (3) two-step probe selection based on correlation with each other (Pearson  $r > 0.3$ ) and



spatial variability of the variogram modelling; (4) averaging across probes; (5) mean-centering normalization across donors; (6) prediction of mRNA levels at voxel level by fitting a variogram model. This rendered spatial brain maps for each gene in MNI maps. Subsequently, ROI values of gene expression were obtained by superimposing the 200 ROI Schaefer atlas,<sup>35</sup> which is also in MNI space, onto each of 18,686 gene expression maps to obtain ROI values. To assess the spatial correspondence of regions' gene expression with that of the average tau-PET uptake in patients with AD, we averaged the 200 Schaefer-ROI tau-PET values across patients in the ADNI training sample, rendering group-average tau-PET ROI values that spatially matched those of the gene expression maps. Next, we computed Spearman correlations between the 200 tau-PET ROI values and the spatially corresponding ROI values of each gene expression map, rendering a distribution of in total 18,686 correlation coefficients. We defined the 5% of correlation coefficients at the lower and higher extreme ends of the distribution of correlation coefficients as those that show a close association between regional gene expression and tau-PET values. The thus selected genes with correlation coefficients in the top 5% of the were retained, and a ROI-to-ROI pairwise Spearman correlation of mRNA expression across those tau-correlated genes were computed to obtain a gene expression similarity matrix.

### 2.3.5 | Neurotransmitter receptors and transporter

A total of 19 receptors and transporters group-averaged PET images were obtained from healthy participants from previous PET tracer studies. The associated receptor or transporter, tracer, sample size, age, and reference region can be found in Table S1. More details of each study were described previously.<sup>20</sup> These receptors and transporters include serotonin (5-HT<sub>1A</sub>, 5-HT<sub>1B</sub>, 5-HT<sub>2A</sub>, 5-HT<sub>4</sub>, 5-HT<sub>6</sub>, 5-HTT), acetylcholine ( $\alpha 4\beta 2$ , M1, VACHT), dopamine (D1, D2, DAT), norepinephrine (NAT), glutamate (mGluR5), histamine(H3), opioid (MOR),  $\gamma$ -aminobutyric acid (GABA<sub>A</sub>), and cannabinoid (CB1).<sup>20</sup> All PET images that had been spatially normalized to the MNI space were downloaded from [https://github.com/netneurolab/hansen\\_receptors](https://github.com/netneurolab/hansen_receptors). For those receptors and transporters with more than one mean image of same tracer (i.e., 5-HT<sub>1B</sub>, D<sub>2</sub>, mGluR<sub>5</sub>, and VACHT), combined densities were calculated as weighted averages. ROI-level values of each PET modality were extracted for each of the 200-Schaefer-atlas ROIs and z-scored. ROI-to-ROI pairwise Spearman correlation matrices were computed across neurotransmitter PET scans.

### 2.3.6 | Assessment of cortical myelin water fraction (MWF)

As described previously,<sup>22</sup> cortical myelination was measured based on a normative MWF atlas obtained from myelin water imaging of 30 healthy individuals (mean age 25 years).<sup>21</sup> The regional mean MWF was extracted within each of the 200 Schaefer-atlas ROIs.

## 2.4 | Calculation of multimodal gradient distance

The concept of spatial "gradient" in the current study refers to the changes in large-scale spatial similarities of brain properties. For example, brain regions can differ with respect to the expression of genes, and the gradient describes the gradual change in the similarity of the gene expression between brain regions. Note that the spatial gradient can be distributed across multiple brain regions, where brain regions distant apart from each other can show high similarity which gradually changes when moving to other brain regions, thus forming a large-scale spatial gradient. The given brain property is maximally different at opposite ends of the gradient, for example, functional connectivity of the default mode network regions is located at one end of the gradient and opposes that of unimodal brain regions on the opposite end.<sup>39</sup> Gradient analysis captures the spatial axis along which such similarities change,<sup>40</sup> and has been applied to multiple brain properties such as gene expression, neurotransmitter distribution, cytoarchitecture, etc.<sup>20,41–43</sup> (for review, see<sup>26</sup>). We generated multimodal gradient maps for all the correlation matrices of functional connectivity, gene expression, amyloid-PET, FDG-PET, neurotransmitter PET using BrainSpace toolbox (<http://brainspace.readthedocs.io/>),<sup>40</sup> as shown in Figure S1. Briefly, the input correlation matrix was thresholded at the sparsity of 10%, and a cosine similarity matrix was computed. To reduce dimensionality, a non-linear diffusion embedding algorithm was employed, allowing for measuring the gradual ordering of a specific feature within a lower-dimensional manifold space.<sup>39</sup> The BrainSpace default setting of the amount of 10 gradients was kept. In order to compute gradient-based distance to the tau-epicenter, we adopted our previously developed approach of connectivity-based distance to tau epicenters.<sup>7</sup> Tau epicenters were defined as top 10% ROIs that showed the highest tau-PET levels among 200 cortical ROIs (i.e.,  $n = 20$ ). For each gradient, tau epicenters at baseline were projected onto gradient maps. The epicenter-based gradient distance was computed as the average absolute difference of the gradient values between tau epicenter ROIs and each ROI across the brain,<sup>44</sup> yielding epicenter-based gradient distance (Figure 1B). The gradient distance values were converted to their reciprocals and then used as the predictors for the predictive model. For the prediction of annual change rate of tau-PET values, the reciprocals of gradient distance were additionally weighted by the baseline regional tau-PET values.

## 2.5 | Gene ontology (GO) enrichment analysis and protein-protein interaction (PPI) network

Next, we aimed to explore the potential biological substrates of the gene expression gradients which were predictive of tau accumulation. In a first step, we determined which of the genes were highly expressed on a given gene-expression gradient that was found to be closely associated with tau-PET. To this end, we performed a spatial correlation using Spearman correlation between the ROI values of the gene expression gradient and the spatially corresponding ROI

values of gene expression of a given single gene. This was done for each single gene that ranked within the top 5% of genes showing a high spatial correlation (i.e., 934 of 18,686 genes, for more details see "Gene expression" section). To account for the spatial autocorrelation, the significance was determined by comparing the empirical spatial similarity (i.e. Spearman rho value) against the null distribution of rho values derived from 1000 spatial permutations ("spin test") according to Vasa's method<sup>45</sup> using the Neuromaps toolbox,<sup>46</sup> where 1000 surrogate maps of the gene expression gradient map were generated while maintaining the spatial autocorrelation. Only genes demonstrating significant correlations ( $p_{spin} < 0.05$ , false discovery rate [FDR] corrected) were retained for subsequent GO enrichment analysis and the PPI network. The GO analysis was performed using the clusterProfiler package implemented in R. The significant GO terms were identified by  $p < 0.05$  corrected by FDR. The data for creating the PPI network were retrieved from the STRING database (<http://string-db.org>) with a high confidence of 0.7. The construction and visualization of the network was performed by Cytoscape 3.3.0. Top 10 nodes with maximal degree centrality were visualized.

## 2.6 | Statistical analyses

Within each sample, baseline demographics were compared between groups using analyses of variance (ANOVAs) or t-test for continuous and chi-squared tests for categorical variables.

### 2.6.1 | Predictor selection with stepwise linear regression

In order to select those predictors that significantly contribute to the prediction of tau-PET levels, a stepwise linear regression was applied. Within the ADNI training sample, all 51 predictors (i.e., 5 imaging modalities  $\times$  10 gradients + 1 myelin MRI template) were iteratively entered into the linear regression model. The sequence of input was determined by the coefficients of spatial correlation between individual predictor and group-average tau-PET map in ADNI training sample. In order to account for similarity due to spatial autocorrelation, we conducted spatial-autocorrelation-preserving permutation tests, where the corrected  $p$ -value ( $p_{spin}$ ) was determined based on the null distribution of  $R^2$  resulting from 1000 spatial permutations. Those predictors that showed a significant improvement of variance explained by the model ( $p_{spin} < 0.05$ ) remained in the model.

### 2.6.2 | Group-level training strategy and cross-validation

For prediction at group level, we trained the models in the ADNI training sample using five-fold cross-validation to predict the spatial pattern of the group-averaged tau-PET levels, and in separate analyses – annual change rates of tau-PET. To determine longitudinal tau-PET change,

we employed linear regression models of tau-PET levels against time from baseline to derive the slopes for each subject. The ADNI training sample was randomly divided into five folds of equal sample size. For each of the five folds, one test fold was held out, and the remaining folds were pooled as training data. The process was repeated for 200 iterations. For each iteration, selected features were fit in a linear regression model. The average parameters across 1000 iterations were used to establish a final linear regression model. The predictive performance of the final model was separately tested in the pooled ADNI training sample, and external samples.

### 2.6.3 | Subject-level prediction

We assessed prediction model performance at the subject level for cross-sectional tau-PET levels and longitudinal tau-PET change rate. For each subject, the epicenter was individually identified on the subject-level tau-PET scan (rather than the group-averaged tau-PET scan), and the gradient distances to epicenters were computed. The distribution of model performance metric ( $R^2$  values) was reported as the means together with the 95% confidence intervals (CIs) across all subjects in each dataset.

The cross-sectional analyses were separately replicated in females and males to evaluate the effect of sex on the results.

## 3 | RESULTS

### 3.1 | Sample characteristics

Baseline demographics and clinical characteristics of the A $\beta$ + participants stratified by status of the presence of cognitive impairment (MCI and AD dementia) are shown in Table 1. The ROI-wise group-average tau-PET SUVRs and rates of change rendered on the brain surface are shown in Figure 2, including the baseline tau epicenters which primarily covered bilateral inferior temporal cortex.

### 3.2 | Spatial gradients to explain group-level tau-PET deposition

Next, we performed stepwise linear regression with spatial-autocorrelation-preserving permutation to select the gradient maps among the different modalities (gene expression, neurotransmitter, functional connectivity, amyloid-PET, FDG PET, myelin image) that significantly contribute to the prediction of group-average tau-PET levels in CN A $\beta$ + and symptomatic A $\beta$ + participants (MCI/dementia). In order to obtain a final predictive model, the coefficients of each selected predictors were estimated and averaged across 1000 cross-validation folds. Epicenters of tau were identified based on the ranking of ROIs of tau-PET images averaged within each group. In CN A $\beta$ + participants, eight predictors consisting of gradients of neurotransmitter, functional connectivity, gene expression, and levels of myelin

**TABLE 1** Sample characteristic.

ADNI	CN A $\beta$ + (n = 153)	MCI A $\beta$ + (n = 128)	Dementia A $\beta$ + (n = 70)	p-value
Age (M/SD)	72.26 (6.68)	72.52 (6.99)	74.32 (7.89)	0.117
Sex (f/m)	93/60	57/71	29/41	0.005
Education (M/SD)	16.58 (2.35)	16.05 (2.55)	15.60 (2.49)	0.016
ApoE $\epsilon$ 4 status(pos/neg)	74/75	71/42	45/21	<0.001
Mean tau-PET follow-up time in years (M/SD) <sup>a</sup>		1.67 (0.79)		
A4/A05	A4 CN A $\beta$ + (n = 388)	A05 MCI A $\beta$ + (n = 83)	A05 Dementia A $\beta$ + (n = 65)	
Age (M/SD)	72.08 (4.79)	73.62 (9.22)	74.43 (9.61)	0.597 <sup>b</sup>
Sex (f/m)	221/167	36/47	35/30	0.271 <sup>b</sup>
Education (M/SD)	16.15 (2.85)	15.63 (2.19)	15.77 (2.19)	0.705 <sup>b</sup>
ApoE4 status(pos/neg)	219/162	42/40	41/22	0.133 <sup>b</sup>
Mean tau-PET follow-up time in years (M/SD) <sup>a</sup>		1.17 (0.38)		

Abbreviation: A $\beta$ , amyloid-beta; ADNI, Alzheimer's Disease Neuroimaging Initiative; ApoE  $\epsilon$ 4, apolipoprotein E  $\epsilon$ 4; CN, cognitively normal; MCI, mild cognitive impairment; PET, positron emission tomography;

<sup>a</sup>Subsample of 58 MCI A $\beta$ + in ADNI, and 46 MCI A $\beta$ + in A05 with follow-up tau-PET available.

<sup>b</sup>Group comparisons between MCI A $\beta$ + and dementia A $\beta$ + in A05 sample.

contributed to the prediction of tau-PET levels (Figure 3A, Table S2). The model combining these gradients explained 76.8% ( $p_{\text{spin}} < 0.001$ ) of the regional tau-PET in the ADNI training sample ( $n = 107$ ), 72.1% ( $p_{\text{spin}} < 0.001$ ) in the unseen ADNI validation sample ( $n = 46$ ), and 67.6% ( $p_{\text{spin}} < 0.001$ ) in the independently recruited sample of the A4 study ( $n = 392$ , Figure 3B).

In MCI/dementia A $\beta$ + participants, 9 predictors consisting of gradients of functional connectivity, neurotransmitter, gene expression, amyloid-PET, FDG-PET, and myelin contributed to the prediction of tau-PET levels (Figure 4A, Table S2). The combined model explained 77.4% ( $p_{\text{spin}} < 0.001$ ) in the ADNI training sample ( $n = 139$ ), 77.7% ( $p_{\text{spin}} < 0.001$ ) in the ADNI validation sample ( $n = 59$ ), and 73.0% ( $p_{\text{spin}} < 0.001$ ) in the A05 study ( $n = 148$ ) (Figure 4B).

The spatial coverage of each of the predictive gradient images with regard to large-scale functional networks is shown in Figures 3C and 4C. Visual inspection shows that each gradient shows a unique distinct spatial distribution, suggesting that the different modalities contribute in a region-specific manner to the tau susceptibility. A substantial proportion of gradients contribute to regional tau-susceptibility across both asymptomatic and symptomatic phases of AD, where a neurotransmitter gradient spanning the limbic versus fronto-parietal-control network space (G2) and the functional connectivity gradients anchored in the motor network (G1). In contrast, gradients of amyloid deposition (G1) were predictive only in the symptomatic phase, suggesting a later involvement of amyloid in underlying spreading of tau-pathology.

The predictors contributing to the prediction of tau-PET levels estimated separately in females and males were largely consistent with those in pooled sample (Figures S2A and S3C). The models explained 71.4%–80.6% variance of the regional tau-PET in females and males across different diagnostic groups and samples (Figures S2B and S3D).

### 3.3 | Multimodal gradient distance-based prediction of subject-level tau-PET levels

Next, we tested whether the group-derived predictive model can explain the individual heterogeneity of tau-PET accumulation across subjects. To this end, we defined for each subject the individual tau epicenters and calculated the gradient distance to individual epicenters, then tested the prediction performance of the group-derived model for subject-level tau-PET SUVRs. The predictive model explained on average 37.4% (95% CI: 30.2%–44.5%), 29.3% (95% CI: 20.6%–38.0%), and 37.0% (95% CI: 33.3%–40.7%) variance of tau-PET levels in CN A $\beta$ + participants from ADNI training, ADNI test and A4 sample respectively (Figure 5A). While in MCI/dementia A $\beta$ + participants, the predictive model increased the proportion of explained variance in ADNI training (mean  $R^2$ : 40.3%; 95% CI: 33.6%–47.1%), ADNI test (mean  $R^2$ : 40.0%; 95% CI: 29.6%–50.5%), and A05 sample (mean  $R^2$ : 41.4%; 95% CI: 34.7%–48.1%, Figure 5B). The sex-specific models explained on average 32.9%–41.7% variance of individual tau-PET levels across different diagnostic groups and samples (Figure S4).



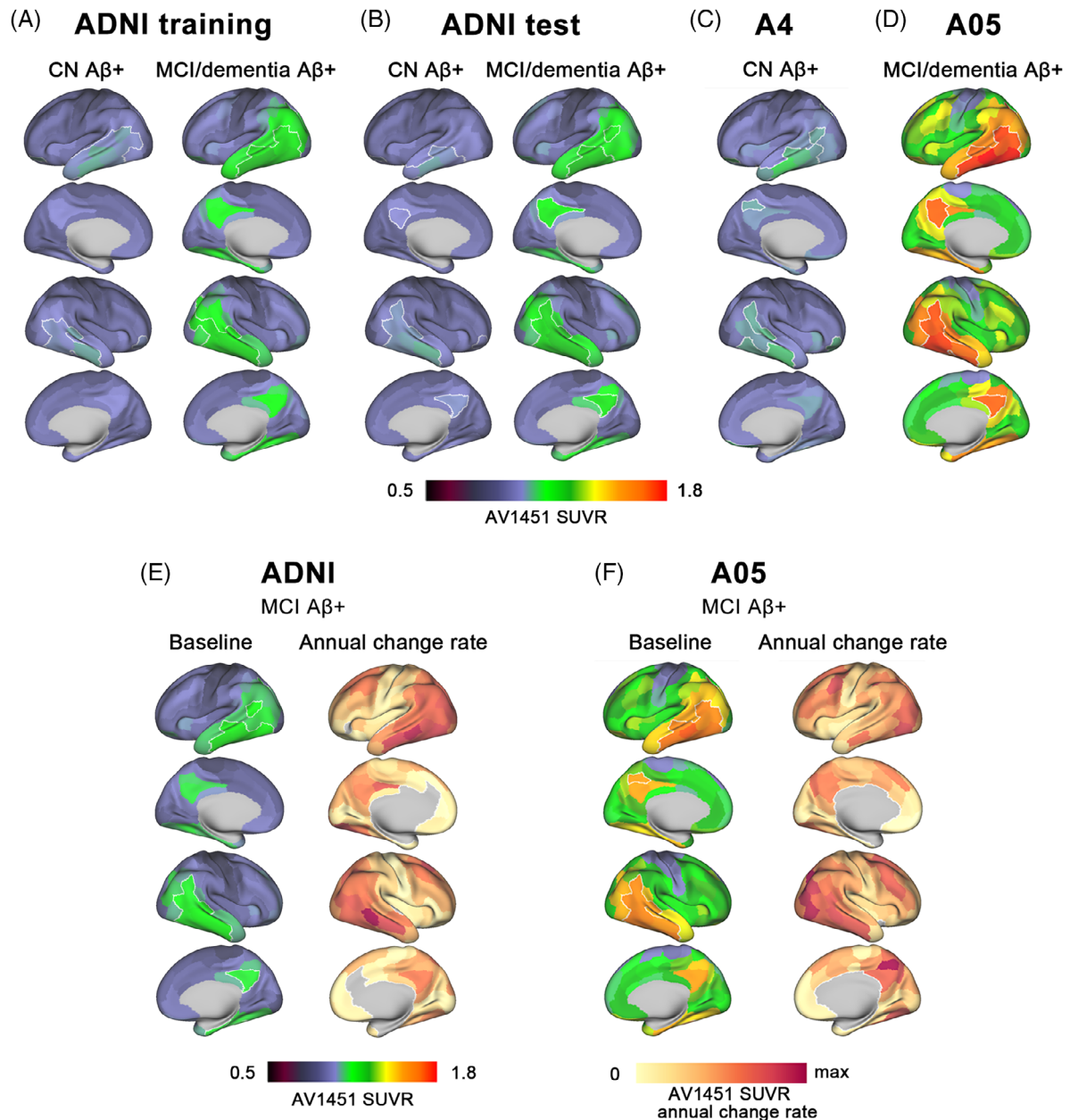


**FIGURE 2** Group-average and annual change rate of tau-PET SUVRs. Average maps of tau-PET SUVRs are shown as continuous values in CN Aβ+ participants, and MCI and dementia Aβ+ participants in ADNI training (A), ADNI test (B), A4 (C), and A05 (D) samples. Average maps of baseline tau-PET SUVRs and annual change rate of tau-PET SUVRs are shown as continuous values in MCI Aβ+ participants in ADNI (e) and A05 (f). Tau epicenters at baseline were shown in outlined white. Aβ, amyloid-beta; ADNI, Alzheimer's Disease Neuroimaging Initiative; CN, cognitively normal; MCI, mild cognitive impairment; PET, positron emission tomography; SUVR, standardized uptake value ratio.

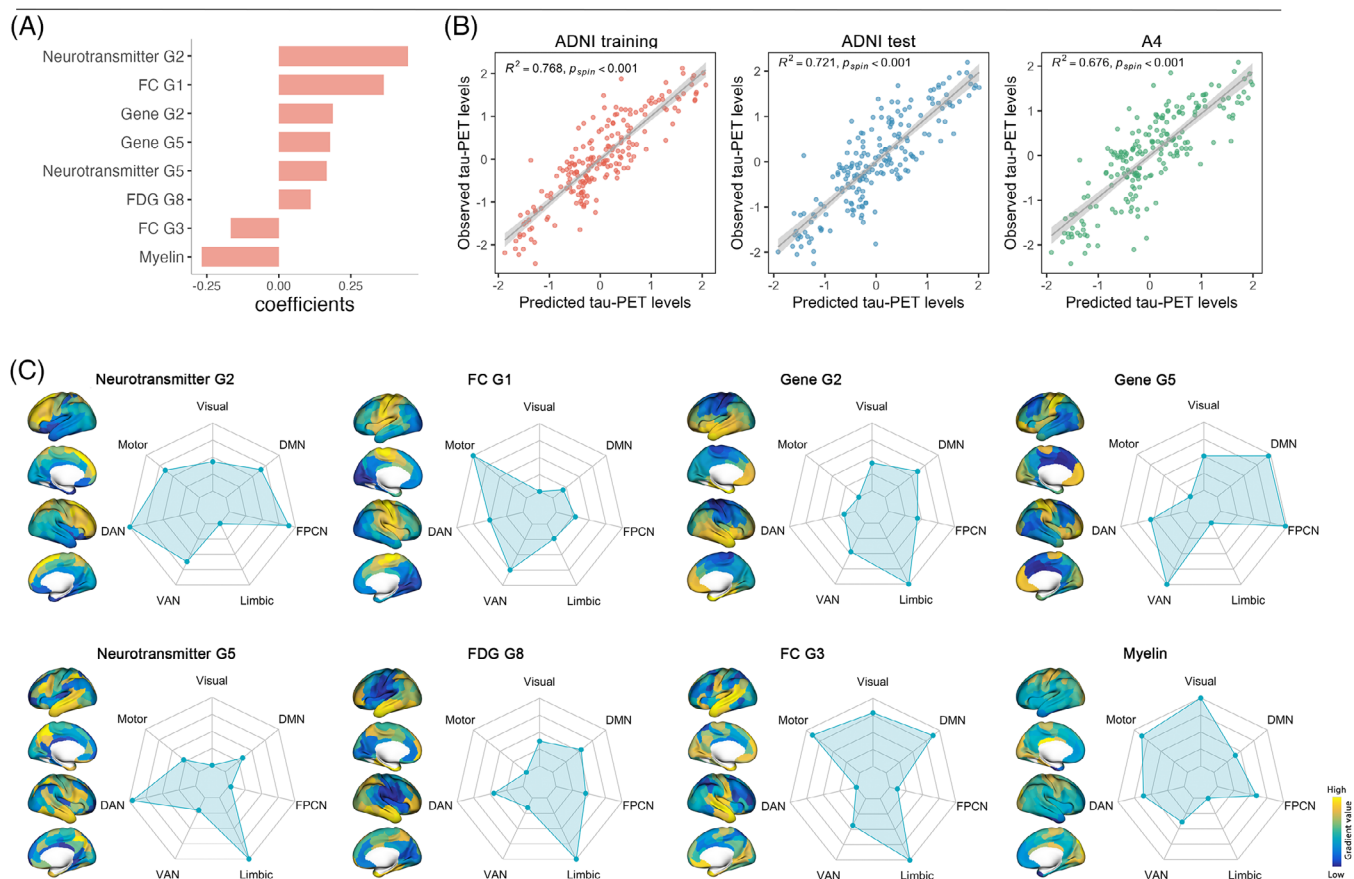
### 3.4 | Multimodal gradient distance-based prediction of group-level tau-PET annual change rates

Lastly, we extended the same approach to longitudinal tau-PET data. Results showed nine predictors consisting of gradients of neurotransmitter, gene expression, FDG-PET, amyloid-PET, and functional connectivity made significant contributions to the prediction of tau-PET annual change rates (Figure 6A, Table S3). The predictive model explained 77.3% and 48.1% variance of tau-PET annual change rates in

MCI Aβ+ participants from ADNI and – for validation—the A05 sample (Figure 6B,C).

### 3.5 | Gene set enrichment analyses and PPI

Finally, we investigated which biological pathways are associated with the gene expression gradients that were found to contribute to the explanation of tau-PET deposition. For gene expression gradient G2 that was associated with early tau deposition in CN Aβ+ individuals,

CN A $\beta$ +

**FIGURE 3** Contributions of multimodal gradient distances to group-mean tau-PET levels. (A) Rank-ordered average coefficients from cross-validation of features selected by stepwise linear regression for predicting group-average tau-PET levels in CN A $\beta$ +. (B) Scatterplots show the association between predicted group-average tau-PET levels against the observed group-average tau-PET levels in CN A $\beta$  participants in ADNI training, ADNI test, and A4 sample. The  $p_{spin}$  stands for the  $p$  values corrected by spatial-autocorrelation-preserving permutation tests. (C) Surface renderings show the spatial pattern of selected features. The radar charts show the distribution of mean gradient values in each canonical functional network. A $\beta$ , amyloid-beta; ADNI, Alzheimer's Disease Neuroimaging Initiative; CN, cognitively normal; PET, positron emission tomography.

GO analysis showed that biological pathways strongly converged on synaptic function (Figure 7A–C). PPI analysis suggested that the genes highly expressed in G2 were associated with synaptic processes, including genes encoding post-synaptic density proteins (i.e., DLG4), pre-synaptic proteins (i.e., SYN1, SYN2, SYT1, STX1A & RIMS1), NMDA receptors (i.e., GRIN2B), growth factor (i.e., brain-derived neurotrophic factor [BDNF]), or neurexin/neuregulin (i.e., NRXN2 & NLGN1, Figure 7D).

## 4 | DISCUSSION

In the current study, we demonstrated that a combination of large-scale connectomics and local brain properties explains a large portion of the regional variability in tau-PET. We reveal that a combination of select gradients of predominantly functional connectivity, neurotransmitter, and gene expression were associated with regional levels of tau deposition at the group and subject-level. Furthermore, our findings

from gene-set enrichment analyses suggested that genes involved in synapse expression may play a vital role in the accumulation of fibrillar tau, supporting the view that the synapse is a potential target for disease modifying treatment in AD.<sup>47</sup> Overall, we present a powerful explanatory model, taking advantage of already existing multimodal imaging maps of brain properties, rendering the approach accessible and cost-effective.

Through the analysis of multimodal gradients, we introduce a uniform approach that allows the integration of different brain properties to explain regional tau levels both at the group level and individual level. We build upon previous connectome-based findings of higher tau in those brain regions that are closely connected to tau-epicenters,<sup>7,48</sup> suggesting that interregional connections provide a pathway for tau to progress during the course of AD.<sup>13</sup> Our findings extend those results on epicenter-based connectivity, showing that tau progresses along large-scale gradients of the brain's connectome. In both asymptomatic and symptomatic A $\beta$  groups, the top gradients with the largest effects size ran along major axis from the limbic network to the dorsal

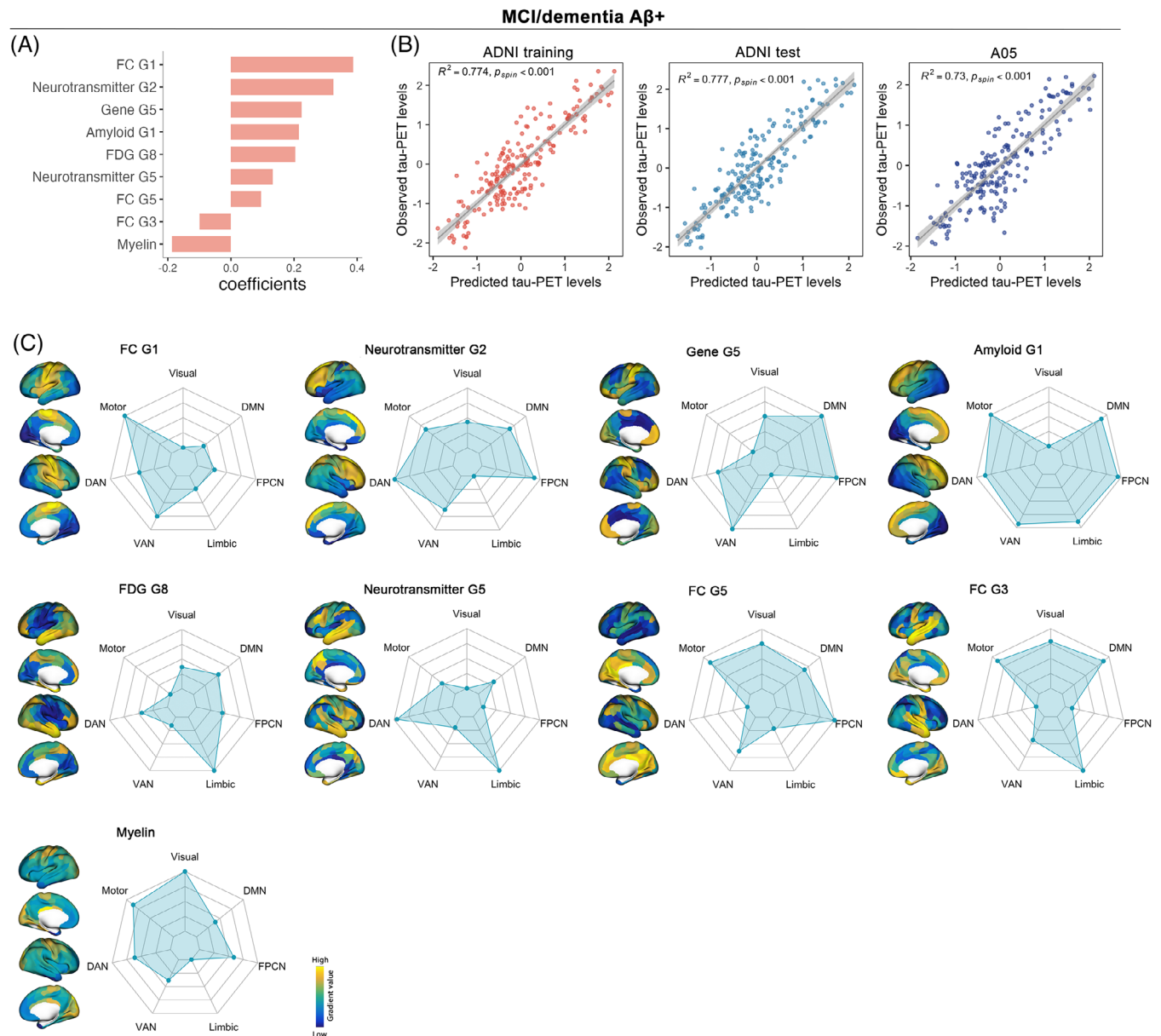


**FIGURE 4** Contributions of multimodal gradient distances to group-mean tau-PET levels. (A) Rank-ordered average coefficients from cross-validation of features selected by stepwise linear regression for predicting group-average tau-PET levels in MCI/dementia Aβ+. (B) Scatterplots show the association between predicted group-average tau-PET levels against the observed group-average tau-PET levels in MCI/dementia Aβ+ participants in ADNI training, ADNI test, and A05 sample. The  $p_{spin}$  stands for the  $p$  values corrected by spatial-autocorrelation-preserving permutation tests. (C) Surface renderings show the spatial pattern of selected features. The radar charts show the distribution of mean gradient values in each canonical functional network. Aβ, amyloid-beta; ADNI, Alzheimer's Disease Neuroimaging Initiative; MCI, mild cognitive impairment; PET, positron emission tomography.

attention and cognitive control networks (neurotransmitter G2, Figures 3C and 4C), motor and ventral attention network (FC G1, Figures 3C and 4C), or the default mode, dorsal attention and cognitive control networks (gene G5, Figures 3C and 4C). Along these gradients, closer distances from the tau epicenter in the limbic network to the posterior default mode network and the orbitofrontal networks were associated with higher susceptibility to tau deposition. These findings are consistent with the observation of higher tau deposition in temporo-parietal and orbitofrontal brain regions in the

symptomatic phase of AD as reported in histochemical brain autopsy and or tau-PET studies.<sup>49,50</sup> Of note, the top predictive functional connectivity gradient (FC G1) resembled the previously reported principal connectome gradient distinguishing between unimodal brain areas in the human brain,<sup>39,51</sup> suggesting that a reproducible principle gradient of the brain's functional connectome related to susceptibility to tau deposition in AD.

In addition to these major gradients which were associated with regional tau deposition both in asymptomatic and symptomatic Aβ+,

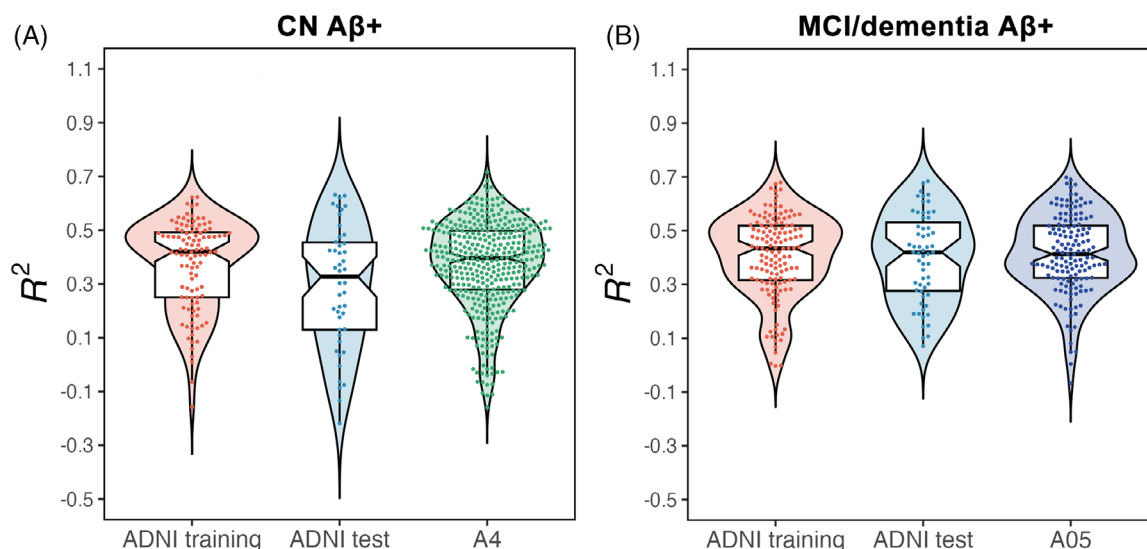


**FIGURE 5** Performances of gradient distance-based prediction of subject-level tau-PET SUVRs. Violin plots show the distribution of  $R^2$  values for prediction of subject-level tau-PET SUVRs using the group-derived multimodal gradient distance-based predictive model in CN A $\beta$ + participants (A) in ADNI training, ADNI test and A4 sample, and MCI/dementia A $\beta$ + participants (B) in ADNI training, ADNI test and A05 sample. A $\beta$ , amyloid-beta; ADNI, Alzheimer's Disease Neuroimaging Initiative; CN, cognitively normal; MCI, mild cognitive impairment; PET, positron emission tomography; SUVR, standardized uptake value ratio.

we also observed disease-stage dependent associations: the gradient of amyloid deposition exhibited explanatory value exclusively in the symptomatic phase of AD, that is, MCI/dementia A $\beta$ + subjects, where the extreme poles of the gradients were situated in the visual cortex versus prefrontal cortex (amyloid G1, Figure 4C). Previous studies suggest that cortical amyloid deposition is pivotal for tau deposition to progress from the medial temporal lobe to higher cortical brain areas in the symptomatic phase of AD,<sup>52,53</sup> whereas tau deposition was confined to the medial temporal lobe in the asymptomatic phase.<sup>54</sup> Therefore, gradients of amyloid deposition may play a role in the progression of tau deposition in more advanced rather than early disease stages of AD when tau is mostly limited to the medial temporal lobe.

To further understand which biological pathways may underlie the regional susceptibility to tau pathology, we conducted a gene set enrichment analysis based on the gradients of gene expression associated with tau-PET. Among the top gene-expression gradients (G2 and G5), the GO analysis yielded a significant biological pathway analysis for G2 but not G5. The G2 gradient was anchored in the limbic network, which opposed the motor network at the other end of the gradient, for which a gene enrichment that strongly converged onto synaptic pathways was observed. Trans-synaptic spreading of tau fibrils has been previously postulated as a major pathomechanism for the spreading of tau pathology in the brain, where not only normal tau but also misfolded tau proteins are released in vesicles via exocytosis and taken up via endocytosis at post-synaptic distal neuron,<sup>55,56</sup> and thus could potentially contribute to the spreading of fibrillar tau between neurons.<sup>57</sup> Because tau is released in an activity-dependent manner,<sup>58</sup> increased neuronal excitation may be associated with increased tau deposition.<sup>59,60</sup> Therefore, altered synapse function could be an important pathomechanism in increased susceptibility to tau spreading. Our

PPI analysis points to key genes such as DLG4 that encode post-synaptic density protein 95 and cluster involving presynaptic vesicle exocytosis and are altered in the AD brain.<sup>61,62</sup> Other key genes of the protein network such as those from the neuroxin/neuregulin (NRXN2 and NLGN1) are cell-adhesion molecules expressed in pre- or postsynaptic terminals and regulate synaptic transmission.<sup>63</sup> In AD, neurexins and neuregulins interact at synapses with A $\beta$  oligomers,<sup>64</sup> and glutamatergic neurons show hyperexcitability and increased neuronal firing in response to A $\beta$ ,<sup>65</sup> which in turn could lead to increased tau transmission within neuronal circuits.<sup>66,67</sup> The proteins including synapsin 1 and synapsin 2 (SYN 1, SYN 2), synaptotagmin 1 (SYT1), and synaptotaxin 1A (STX1A) are all synaptic proteins involved in the endocytosis of synaptic vesicles or synaptogenesis, that is, key mechanisms thought to underlie the trans-synaptic transmission of tau fibrils.<sup>55,58,68</sup> For tau, previous studies showed that optogenetic stimulation of neuronal activity enhanced the release of tau and was associated with higher tau pathology in vivo,<sup>60</sup> suggesting that fibrillar tau may spread in a neural activity-dependent manner. At the synaptic level, the synaptic vesicle release is regulated by proteins such as synapsin in an activity dependent manner,<sup>69</sup> and neurotrophic factors such as BDNF potentiates synaptic vesicle trafficking in interaction with synapsin.<sup>70</sup> A polymorphism in the BDNF gene including the Val66Met haplotype, has been associated with increased levels of pathologic tau in patients with autosomal-dominant AD,<sup>71</sup> but the exact mechanism of neuronal hyperactivation on mediation such a BDNF effect on core AD pathologies remains to be clarified.<sup>72,73</sup> In summary, synaptic processes may play a crucial pathomechanistic role in the spreading of tau pathology in AD.<sup>55</sup>

Overall, our results suggest that a multifold of brain properties modulate the susceptibility to tau pathology, where the combination of



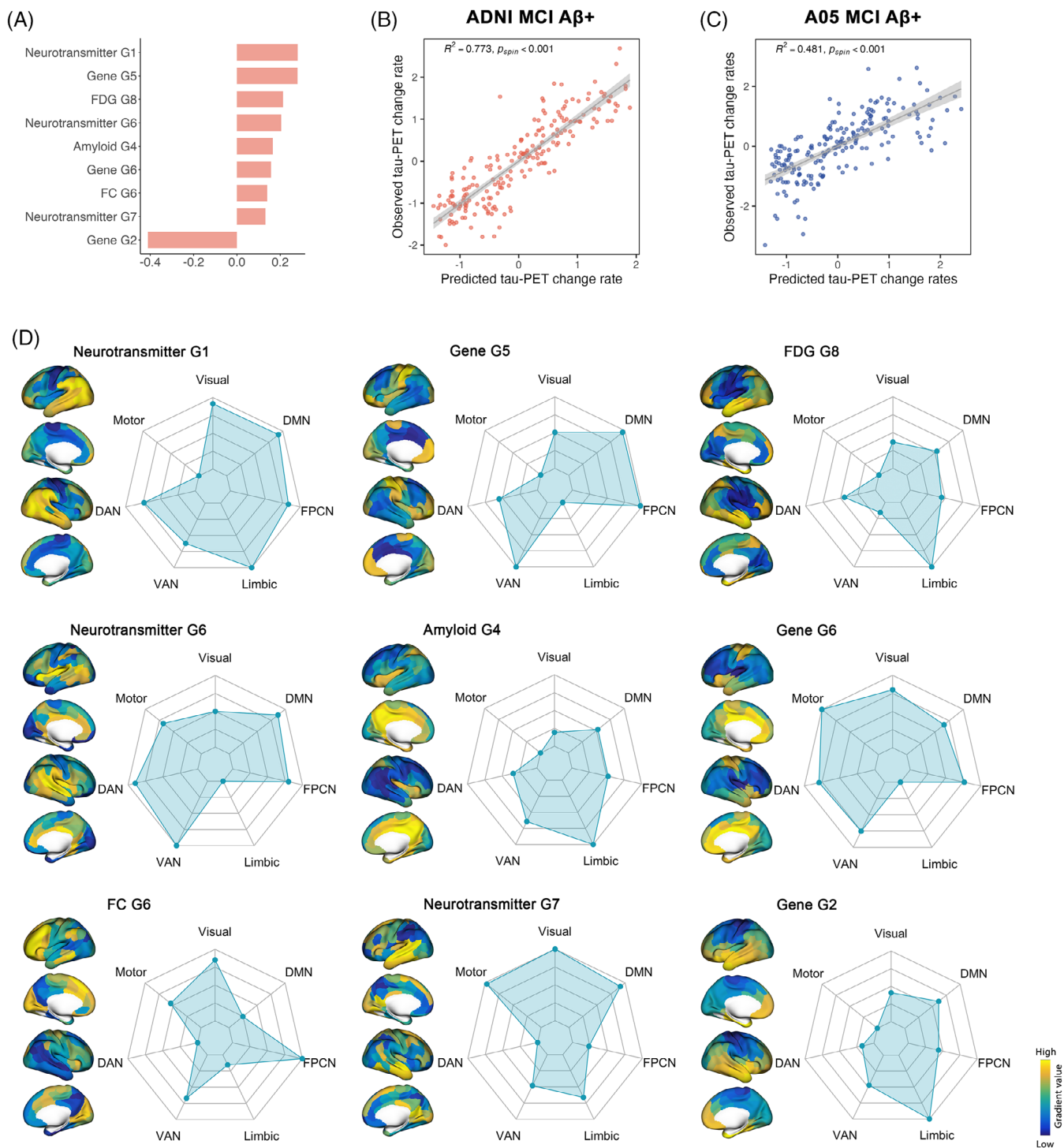


**FIGURE 6** Contributions of multimodal gradient distances to group-mean tau-PET annual change rates and prediction performances. (a) Rank-ordered average coefficients from cross-validation of features selected by stepwise linear regression for predicting group-average tau-PET annual change rates in MCI Aβ+ participants from ADNI. The scatterplots show the association between predicted group-average tau-PET levels against the observed group-average tau-PET levels in MCI Aβ+ participants in ADNI (B) and A05 (C). The  $p_{spin}$  stands for the  $p$  values corrected by spatial-autocorrelation-preserving permutation tests. (C) Surface renderings show the spatial pattern of selected features. The radar charts show the distribution of mean gradient values in each canonical functional network. Aβ, amyloid-beta; ADNI, Alzheimer's Disease Neuroimaging Initiative; MCI, mild cognitive impairment; PET, positron emission tomography.



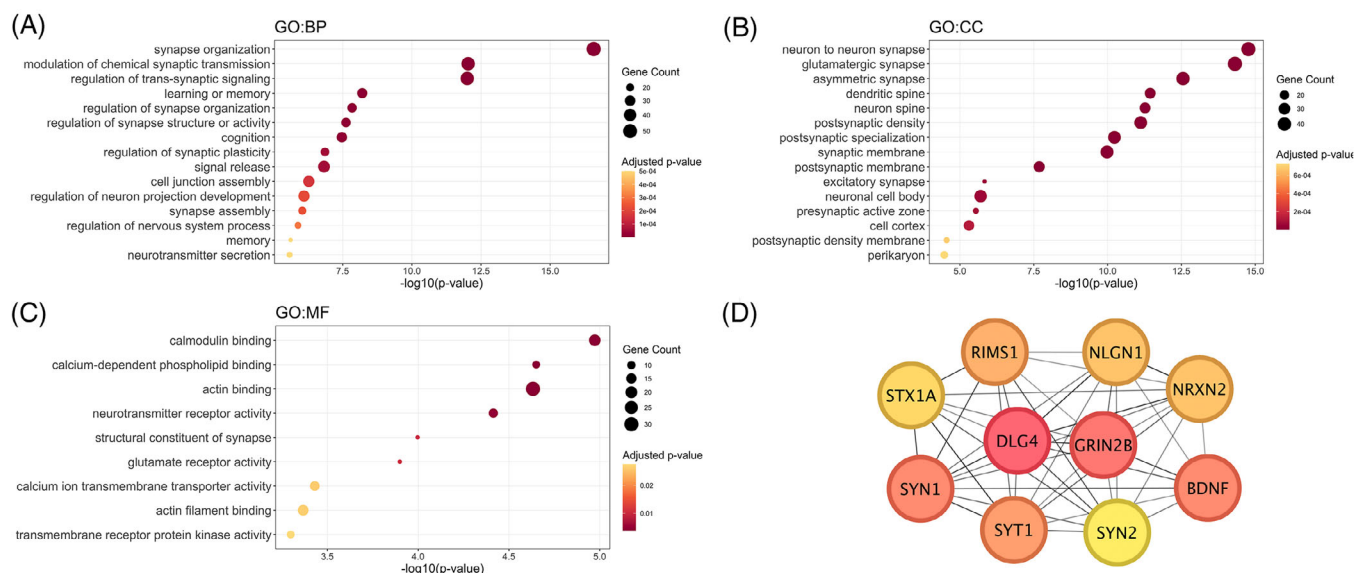


**FIGURE 7** Gene expression profiles associated with gene expression gradient 2. Bubble plots show results of GO analyses for biological process (A), cellular component (B), and molecular function (C). The dots represent the GO terms corrected for multiple comparisons (FDR-corrected at  $p < 0.05$ ). Gene count means the number of genes in that pathway. (D) Protein-protein interaction network shows the top 10 hub genes identified with a maximal centrality generated by Cytoscape. FDR, false discovery rate; GO, gene ontology.

different gradient images provide a powerful model to explain regional susceptibility to tau pathology. Our approach has several strengths as it can be applied based on a priori maps of brain properties and thus is not dependent on multimodal imaging in each patient in order to predict longitudinal tau when applied at the individual level. We used extensive cross-validation in independently recruited samples to guard against overfitting and to test the reproducibility of our findings. For the interpretation of our results, several caveats however, also need to be taken into account. First, we present a model that can be used to explain and predict regional differences in tau pathology rather than demonstrate a causative relationship, which need to be interrogated in future experimental studies. Second, previous studies described subtypes of AD which may show differences spatial trajectories of brain alterations including tau pathology in AD.<sup>9</sup> However, rather than focusing on subtypes, which so far lack a consensus definition,<sup>74</sup> our approach of defining epicenters of tau pathology as a point of reference allows the flexible adaption at the individual level, that may capture interindividual variability without requiring the classification of subjects into subtypes. It is important to address in future studies those factors that drive inter-individual differences in regional tau deposition. Furthermore, we acknowledge that molecular brain properties such as gene expression may change as part of normal aging, and thus should have ideally been obtained in elderly individuals to explain regional susceptibility to tau pathology. Yet, the assessment of such multimodal brain properties in elderly subjects was beyond the scope of the current study. Lastly, we like to point out that factors of diversity including sex-specific and ethnic background may be potential modifiers. The templates of brain features such as gene expression employed here however, did not lend themselves to investigate such systematic effects but require larger sample sizes to detect any potential mod-

ifying effects. However, the current results provide high explanatory values across multiple samples which demonstrate the utility of the current method to uncover brain signatures that underlie susceptibility to tau pathology.

## ACKNOWLEDGMENTS

We appreciate the ADNI, 18F-AV-1451-A05, and A4 study for data sharing. Y.L. receives the research funding from the National Natural Science Foundation of China (NO. 82202131). This study was funded by Bundesministerium für Bildung und Forschung (BMBF, ERA PerMed, 01KU2203). ADNI data collection and sharing for this project was funded by the ADNI (National Institutes of Health Grant U01 AG024904) and DOD ADNI (Department of Defense award number W81XWH-12-2-0012). ADNI is funded by the National Institute on Aging, the National Institute of Biomedical Imaging, and Bioengineering, and through contributions from the following: AbbVie, Alzheimer's Association; Alzheimer's Drug Discovery Foundation; Araclon Biotech; BioClinica, Inc.; Biogen; Bristol-Myers Squibb Company; CereSpir, Inc.; Cogstate; Eisai Inc.; Elan Pharmaceuticals, Inc.; Eli Lilly and Company; EuroImmun; F. Hoffmann-La Roche Ltd and its affiliated company Genentech, Inc.; Fujirebio; GE Healthcare; IXICO Ltd.; Janssen Alzheimer Immunotherapy Research & Development, LLC.; Johnson & Johnson Pharmaceutical Research & Development LLC.; Lumosity; Lundbeck; Merck & Co., Inc.; Meso Scale Diagnostics, LLC.; NeuroRx Research; Neurotrack Technologies; Novartis Pharmaceuticals Corporation; Pfizer Inc.; Piramal Imaging; Servier; Takeda Pharmaceutical Company; and Transition Therapeutics. The Canadian Institutes of Health Research is providing funds to support ADNI clinical sites in Canada. Private sector contributions are facilitated by the Foundation for the National Institutes of Health ([www.fnih.org](http://www.fnih.org)).

## CONFLICT OF INTEREST STATEMENT

M.E. and N.F. receive research funding from Eli Lilly. All other authors reported no conflict of interest. Author disclosures are available in the [Supporting Information](#).

## CONSENT STATEMENT

All subjects or their authorized representatives provided signed informed consent. Ethical approval and written informed consent were obtained by ADNI, A05, and A4 investigators.

## ORCID

Michael Ewers  <https://orcid.org/0000-0001-5231-1714>

## REFERENCES

- Alzheimer's Association. 2023 Alzheimer's disease facts and figures. *Alzheimers Dement*. 2023;19(4):1598-1695. doi:10.1002/alz.13016
- Ossenkoppele R, Reimand J, Smith R, et al. Tau PET correlates with different Alzheimer's disease-related features compared to CSF and plasma p-tau biomarkers. *EMBO Mol Med*. 2021;13(8):e14398. doi:10.15252/emmm.202114398
- Braak H, Braak E. Neuropathological staging of Alzheimer-related changes. *Acta Neuropathologica*. 1991;82(4):239-59.
- Kaufman SK, Del Tredici K, Thomas TL, Braak H, Diamond MI. Tau seeding activity begins in the transentorhinal/entorhinal regions and anticipates phospho-tau pathology in Alzheimer's disease and PART. *Acta neuropathologica*. 2018;136(1):57-67. doi:10.1007/s00401-018-1855-6
- Chen SD, Lu JY, Li HQ, et al. Staging tau pathology with tau PET in Alzheimer's disease: a longitudinal study. *Transl Psychiatry*. 2021;11(1):483. doi:10.1038/s41398-021-01602-5
- Yu M, Sporns O, Saykin AJ. The human connectome in Alzheimer disease - relationship to biomarkers and genetics. *Nat Rev Neurol*. 2021;17(9):545-563. doi:10.1038/s41582-021-00529-1
- Franzmeier N, Dewenter A, Frontzkowski L, et al. Patient-centered connectivity-based prediction of tau pathology spread in Alzheimer's disease. *Sci Adv*. 2020;6(48):eabd1327. doi:10.1126/sciadv.abd1327
- Franzmeier N, Neitzel J, Rubinski A, et al. Functional brain architecture is associated with the rate of tau accumulation in Alzheimer's disease. *Nat Commun*. 2020;11(1):347. doi:10.1038/s41467-019-14159-1
- Vogel JW, Young AL, Oxtoby NP, et al. Four distinct trajectories of tau deposition identified in Alzheimer's disease. *Nature medicine*. 2021;27(5):871-881. doi:10.1038/s41591-021-01309-6
- Calafate S, Buist A, Miskiewicz K, et al. Synaptic Contacts Enhance Cell-to-Cell Tau Pathology Propagation. *Cell Rep*. 2015;11(8):1176-1183. doi:10.1016/j.celrep.2015.04.043
- Mate De Gerando A, Welikovitsh LA, Khasnavis A, et al. Tau seeding and spreading in vivo is supported by both AD-derived fibrillar and oligomeric tau. *Acta Neuropathol*. 2023;146(2):191-210. doi:10.1007/s00401-023-02600-1
- Meisl G, Hidari E, Allinson K, et al. In vivo rate-determining steps of tau seed accumulation in Alzheimer's disease. *Sci Adv*. 2021;7(44):eabh1448. doi:10.1126/sciadv.abh1448
- Vogel JW, Corriveau-Lecavalier N, Franzmeier N, et al. Connectome-based modelling of neurodegenerative diseases: towards precision medicine and mechanistic insight. *Nat Rev Neurosci*. 2023;24(10):620-639. doi:10.1038/s41583-023-00731-8
- Sepulcre J, Grothe MJ, d'Oleire Uquillas F, et al. Neurogenetic contributions to amyloid beta and tau spreading in the human cortex. *Nat Med*. 2018;24(12):1910-1918. doi:10.1038/s41591-018-0206-4
- Neitzel J, Franzmeier N, Rubinski A, et al. KL-VS heterozygosity is associated with lower amyloid-dependent tau accumulation and memory impairment in Alzheimer's disease. *Nat Commun*. 2021;12(1):3825. doi:10.1038/s41467-021-23755-z
- Grothe MJ, Sepulcre J, Gonzalez-Escamilla G, et al. Molecular properties underlying regional vulnerability to Alzheimer's disease pathology. *Brain*. 2018;141(9):2755-2771. doi:10.1093/brain/awy189
- Sepulcre J, Grothe MJ, Uquillas FdO, et al. Neurogenetic contributions to amyloid beta and tau spreading in the human cortex. *Nature medicine*. 2018;24(12):1910. doi:10.1038/s41591-018-0206-4
- Zheng L, Rubinski A, Denecke J, et al. Combined connectomics, MAPT gene expression, and amyloid deposition to explain regional tau deposition in Alzheimer disease. *Annals of neurology*. 2024;95(2):274-287. doi:10.1002/ana.26818
- Hawrylycz MJ, Lein ES, Guillozet-Bongaarts AL, et al. An anatomically comprehensive atlas of the adult human brain transcriptome. *Nature*. 2012;489(7416):391-399.
- Hansen JY, Shafiei G, Markello RD, et al. Mapping neurotransmitter systems to the structural and functional organization of the human neocortex. *Nature neuroscience*. 2022;25(11):1569-1581. doi:10.1038/s41593-022-01186-3
- Liu H, Rubino C, Dvorak AV, et al. Myelin water atlas: a template for myelin distribution in the brain. *J Neuroimaging*. 2019;29(6):699-706. doi:10.1111/jon.12657
- Rubinski A, Franzmeier N, Dewenter A, et al. Higher levels of myelin are associated with higher resistance against tau pathology in Alzheimer's disease. *Alzheimers Res Ther*. 2022;14(1):139. doi:10.1186/s13195-022-01074-9
- Lindhout FW, Krienen FM, Pollard KS, Lancaster MA. A molecular and cellular perspective on human brain evolution and tempo. *Nature*. 2024;630(8017):596-608. doi:10.1038/s41586-024-07521-x
- Hansen JY, Shafiei G, Vogel JW, et al. Local molecular and global connectomic contributions to cross-disorder cortical abnormalities. *Nat Commun*. 2022;13(1):4682. doi:10.1038/s41467-022-32420-y
- Segal A, Parkes L, Aquino K, et al. Regional, circuit and network heterogeneity of brain abnormalities in psychiatric disorders. *Nature neuroscience*. 2023;26(9):1613-1629. doi:10.1038/s41593-023-01404-6
- Huntenburg JM, Bazin PL, Margulies DS. Large-scale gradients in human cortical organization. *Trends in cognitive sciences*. 2018;22(1):21-31. doi:10.1016/j.tics.2017.11.002
- Weiner MW, Veitch DP, Aisen PS, et al. The Alzheimer's Disease Neuroimaging Initiative 3: continued innovation for clinical trial improvement. *Alzheimers Dement*. 2017;13(5):561-571. doi:10.1016/j.jalz.2016.10.006
- Petersen RC, Aisen PS, Beckett LA, et al. Alzheimer's Disease Neuroimaging Initiative (ADNI): clinical characterization. *Neurology*. 2010;74(3):201-9. doi:10.1212/WNL.0b013e3181cb3e25
- Sperling RA, Rentz DM, Johnson KA, et al. The A4 study: stopping AD before symptoms begin? *Science translational medicine*. 2014;6(228):228fs13. doi:10.1126/scitranslmed.3007941
- Sperling RA, Donohue MC, Raman R, et al. Trial of solanezumab in pre-clinical Alzheimer's disease. *N Engl J Med*. 2023;389(12):1096-1107. doi:10.1056/NEJMoa2305032
- Pontecorvo MJ, Devous MD, Kennedy I, et al. A multicentre longitudinal study of flortaucipir (18F) in normal ageing, mild cognitive impairment and Alzheimer's disease dementia. *Brain*. 2019;142(6):1723-1735. doi:10.1093/brain/awz090
- Pontecorvo MJ, Devous MD, Sr., Navitsky M, et al. Relationships between flortaucipir PET tau binding and amyloid burden, clinical diagnosis, age and cognition. *Brain*. 2017;140(3):748-763. doi:10.1093/brain/aww334
- Baker SL, Maass A, Jagust WJ. Considerations and code for partial volume correcting [(18)F]-AV-1451 tau PET data. *Data Brief*. 2017;15:648-657. doi:10.1016/j.dib.2017.10.024
- Franzmeier N, Duering M, Weiner M, Dichgans M, Ewers M; Alzheimer's Disease Neuroimaging I. Left frontal cortex connectivity

- underlies cognitive reserve in prodromal Alzheimer disease. *Neurology*. 2017;88(11):1054-1061. doi:[10.1212/WNL.0000000000003711](https://doi.org/10.1212/WNL.0000000000003711)
35. Schaefer A, Kong R, Gordon EM, et al. Local-global parcellation of the human cerebral cortex from intrinsic functional connectivity MRI. *Cereb Cortex*. 2018;28(9):3095-3114. doi:[10.1093/cercor/bhx179](https://doi.org/10.1093/cercor/bhx179)
  36. Fortin J-P, Parker D, Tunç B, et al. Harmonization of multi-site diffusion tensor imaging data. *NeuroImage*. 2017;161:149-170. doi:[10.1016/j.neuroimage.2017.08.047](https://doi.org/10.1016/j.neuroimage.2017.08.047)
  37. Gryglewski G, Seiger R, James GM, et al. Spatial analysis and high resolution mapping of the human whole-brain transcriptome for integrative analysis in neuroimaging. *NeuroImage*. 2018;176:259-267. doi:[10.1016/j.neuroimage.2018.04.068](https://doi.org/10.1016/j.neuroimage.2018.04.068)
  38. Shen EH, Overly CC, Jones AR. The Allen Human Brain Atlas: comprehensive gene expression mapping of the human brain. *Trends Neurosci*. 2012;35(12):711-714. doi:[10.1016/j.tins.2012.09.005](https://doi.org/10.1016/j.tins.2012.09.005)
  39. Margulies DS, Ghosh SS, Goulas A, et al. Situating the default-mode network along a principal gradient of macroscale cortical organization. *Proc Natl Acad Sci U S A*. 2016;113(44):12574-12579. doi:[10.1073/pnas.1608282113](https://doi.org/10.1073/pnas.1608282113)
  40. Vos de Wael R, Benkarim O, Paquola C, et al. BrainSpace: a toolbox for the analysis of macroscale gradients in neuroimaging and connectomics datasets. *Commun Biol*. 2020;3(1):103. doi:[10.1038/s42003-020-0794-7](https://doi.org/10.1038/s42003-020-0794-7)
  41. Fulcher BD, Murray JD, Zerbi V, Wang XJ. Multimodal gradients across mouse cortex. *Proc Natl Acad Sci U S A*. 2019;116(10):4689-4695. doi:[10.1073/pnas.1814144116](https://doi.org/10.1073/pnas.1814144116)
  42. Burt JB, Demirtas M, Eckner WJ, et al. Hierarchy of transcriptomic specialization across human cortex captured by structural neuroimaging topography. *Nat Neurosci*. 2018;21(9):1251-1259. doi:[10.1038/s41593-018-0195-0](https://doi.org/10.1038/s41593-018-0195-0)
  43. Huntenburg JM, Bazin P-L, Margulies DS. Large-scale gradients in human cortical organization. *Trends in cognitive sciences*. 2018;22(1):21-31.
  44. Bayrak S, Khalil AA, Villringer K, et al. The impact of ischemic stroke on connectivity gradients. *NeuroImage Clin*. 2019;24:101947. doi:[10.1016/j.nicl.2019.101947](https://doi.org/10.1016/j.nicl.2019.101947)
  45. Vasa F, Seidlitz J, Romero-Garcia R, et al. Adolescent tuning of association cortex in human structural brain networks. *Cereb Cortex*. 2018;28(1):281-294. doi:[10.1093/cercor/bhx249](https://doi.org/10.1093/cercor/bhx249)
  46. Markello RD, Hansen JY, Liu ZQ, et al. Neuromaps: structural and functional interpretation of brain maps. *Nat Methods*. 2022;19(11):1472-1479. doi:[10.1038/s41592-022-01625-w](https://doi.org/10.1038/s41592-022-01625-w)
  47. Peng L, Bestard-Lorigados I, Song W. The synapse as a treatment avenue for Alzheimer's Disease. *Mol Psychiatry*. 2022;27(7):2940-2949. doi:[10.1038/s41380-022-01565-z](https://doi.org/10.1038/s41380-022-01565-z)
  48. Vogel JW, Iturria-Medina Y, Strandberg OT, et al. Spread of pathological tau proteins through communicating neurons in human Alzheimer's disease. *Nat Commun*. 2020;11(1):2612. doi:[10.1038/s41467-020-15701-2](https://doi.org/10.1038/s41467-020-15701-2)
  49. Therriault J, Pascoal TA, Lussier FZ, et al. Biomarker modeling of Alzheimer's disease using PET-based Braak staging. *Nat Aging*. 2022;2(6):526-535. doi:[10.1038/s43587-022-00204-0](https://doi.org/10.1038/s43587-022-00204-0)
  50. Braak H, Braak E. Frequency of stages of Alzheimer-related lesions in different age categories. *Neurobiol Aging*. 1997;18(4):351-357.
  51. Labache L, Ge T, Yeo BTT, Holmes AJ. Language network lateralization is reflected throughout the macroscale functional organization of cortex. *Nat Commun*. 2023;14(1):3405. doi:[10.1038/s41467-023-39131-y](https://doi.org/10.1038/s41467-023-39131-y)
  52. Lee WJ, Brown JA, Kim HR, et al. Regional Abeta-tau interactions promote onset and acceleration of Alzheimer's disease tau spreading. *Neuron*. 2022;110(12):1932-1943 e5. doi:[10.1016/j.neuron.2022.03.034](https://doi.org/10.1016/j.neuron.2022.03.034)
  53. Sanchez JS, Becker JA, Jacobs HIL, et al. The cortical origin and initial spread of medial temporal tauopathy in Alzheimer's disease assessed with positron emission tomography. *Science translational medicine*. 2021;13(577):eabc0655. doi:[10.1126/scitranslmed.abc0655](https://doi.org/10.1126/scitranslmed.abc0655)
  54. Schöll M, Lockhart SN, Schonhaut DR, et al. PET imaging of tau deposition in the aging human brain. *Neuron*. 2016;89(5):971-982.
  55. Colom-Cadena M, Davies C, Sirisi S, et al. Synaptic oligomeric tau in Alzheimer's disease - a potential culprit in the spread of tau pathology through the brain. *Neuron*. 2023;111(14):2170-2183 e6. doi:[10.1016/j.neuron.2023.04.020](https://doi.org/10.1016/j.neuron.2023.04.020)
  56. Kfoury N, Holmes BB, Jiang H, Holtzman DM, Diamond MI. Trans-cellular propagation of Tau aggregation by fibrillar species. *J Biol Chem*. 2012;287(23):19440-19451. doi:[10.1074/jbc.M112.346072](https://doi.org/10.1074/jbc.M112.346072)
  57. de Calignon A, Polydoro M, Suarez-Calvet M, et al. Propagation of tau pathology in a model of early Alzheimer's disease. *Neuron*. 2012;73(4):685-697. doi:[10.1016/j.neuron.2011.11.033](https://doi.org/10.1016/j.neuron.2011.11.033)
  58. Pooler AM, Phillips EC, Lau DH, Noble W, Hanger DP. Physiological release of endogenous tau is stimulated by neuronal activity. *EMBO Rep*. 2013;14(4):389-394. doi:[10.1038/embor.2013.15](https://doi.org/10.1038/embor.2013.15)
  59. Ranasinghe KG, Verma P, Cai C, et al. Altered excitatory and inhibitory neuronal subpopulation parameters are distinctly associated with tau and amyloid in Alzheimer's disease. *Elife*. 2022;11:e77850. doi:[10.7554/eLife.77850](https://doi.org/10.7554/eLife.77850)
  60. Wu JW, Hussaini SA, Bastille IM, et al. Neuronal activity enhances tau propagation and tau pathology in vivo. *Nat Neurosci*. 2016;19(8):1085-1092. doi:[10.1038/nn.4328](https://doi.org/10.1038/nn.4328)
  61. Xu J, Patassini S, Rustogi N, et al. Regional protein expression in human Alzheimer's brain correlates with disease severity. *Commun Biol*. 2019;2:43. doi:[10.1038/s42003-018-0254-9](https://doi.org/10.1038/s42003-018-0254-9)
  62. Williams JB, Cao Q, Yan Z. Transcriptomic analysis of human brains with Alzheimer's disease reveals the altered expression of synaptic genes linked to cognitive deficits. *Brain Commun*. 2021;3(3):fcab123. doi:[10.1093/braincomms/fcab123](https://doi.org/10.1093/braincomms/fcab123)
  63. Sudhof TC. Neuroligins and neuroligins link synaptic function to cognitive disease. *Nature*. 2008;455(7215):903-911. doi:[10.1038/nature07456](https://doi.org/10.1038/nature07456)
  64. Brito-Moreira J, Lourenco MV, Oliveira MM, et al. Interaction of amyloid-beta (Aβ) oligomers with neuroligin 2α and neuroligin 1 mediates synapse damage and memory loss in mice. *J Biol Chem*. 2017;292(18):7327-7337. doi:[10.1074/jbc.M116.761189](https://doi.org/10.1074/jbc.M116.761189)
  65. Zott B, Simon MM, Hong W, et al. A vicious cycle of beta amyloid-dependent neuronal hyperactivation. *Science*. 2019;365(6453):559-565. doi:[10.1126/science.aay0198](https://doi.org/10.1126/science.aay0198)
  66. Giorgio J, Adams JN, Maass A, Jagust WJ, Breakspear M. Amyloid induced hyperexcitability in default mode network drives medial temporal hyperactivity and early tau accumulation. *Neuron*. 2024;112(4):676-686 e4. doi:[10.1016/j.neuron.2023.11.014](https://doi.org/10.1016/j.neuron.2023.11.014)
  67. Busche MA, Hyman BT. Synergy between amyloid-beta and tau in Alzheimer's disease. *Nature neuroscience*. 2020;23(10):1183-1193. doi:[10.1038/s41593-020-0687-6](https://doi.org/10.1038/s41593-020-0687-6)
  68. Fontaine SN, Zheng D, Sabbagh JJ, et al. DnaJ/Hsc70 chaperone complexes control the extracellular release of neurodegenerative-associated proteins. *EMBO J*. 2016;35(14):1537-1549. doi:[10.15252/embj.201593489](https://doi.org/10.15252/embj.201593489)
  69. Mirza FJ, Zahid S. The Role of Synapsins in Neurological Disorders. *Neurosci Bull*. 2018;34(2):349-358. doi:[10.1007/s12264-017-0201-7](https://doi.org/10.1007/s12264-017-0201-7)
  70. Valente P, Casagrande S, Nieuws T, et al. Site-specific synapsin I phosphorylation participates in the expression of post-tetanic potentiation and its enhancement by BDNF. *J Neurosci*. 2012;32(17):5868-5879. doi:[10.1523/JNEUROSCI.5275-11.2012](https://doi.org/10.1523/JNEUROSCI.5275-11.2012)
  71. Lim YY, Maruff P, Barthelemy NR, et al. Association of BDNF Val66Met with Tau hyperphosphorylation and cognition in dominantly inherited Alzheimer disease. *JAMA Neurol*. 2022;79(3):261-270. doi:[10.1001/jamaneurol.2021.5181](https://doi.org/10.1001/jamaneurol.2021.5181)
  72. Egan MF, Kojima M, Callicott JH, et al. The BDNF val66met polymorphism affects activity-dependent secretion of BDNF and human memory and hippocampal function. *Cell*. 2003;112(2):257-269.
  73. Franzmeier N, Ren J, Damm A, et al. The BDNF(Val66Met) SNP modulates the association between beta-amyloid and hippocampal discon-

nection in Alzheimer's disease. *Mol Psychiatry*. 2021;26(2):614-628. doi:[10.1038/s41380-019-0404-6](https://doi.org/10.1038/s41380-019-0404-6)

74. Ferreira D, Nordberg A, Westman E. Biological subtypes of Alzheimer disease: a systematic review and meta-analysis. *Neurology*. 2020;94(10):436-448. doi:[10.1212/WNL.00000000000009058](https://doi.org/10.1212/WNL.00000000000009058)

## SUPPORTING INFORMATION

Additional supporting information can be found online in the Supporting Information section at the end of this article.

**How to cite this article:** Luan Y, Zheng L, Denecke J, et al.; for the Alzheimer's Disease Neuroimaging Initiative (ADNI). Multimodal spatial gradients to explain regional susceptibility to fibrillar tau in Alzheimer's disease. *Alzheimer's Dement*. 2025;21:e70170. <https://doi.org/10.1002/alz.70170>